Oxygen-diffusion-driven oxidation behavior and tracking areas visualized by X-ray spectro-ptychography with unsupervised learning

Oxygen-diffusion-driven oxidation behavior and tracking areas visualized by X-ray spectro-ptychography with unsupervised learning

Makoto Hirose[1,2], Nozomu Ishiguro[2], Kei Shimomura[1,2], Duong-Nguyen Nguyen[3], Hirosuke Matsui[4], Hieu Chi Dam[3,5], Mizuki Tada[2,4] & Yukio Takahashi [1,2,6]

Oxygen storage and release with oxygen diffusion in the bulk of the cerium–zirconium solid solution oxide $Ce_2Zr_2O_x$ ($x = 7$–8), which possesses an atomically ordered arrangement of cerium and zirconium atoms, is the key to three-way exhaust catalysis. Oxygen storage proceeds via heterogeneous oxygen diffusion into the vacant sites of $Ce_2Zr_2O_7$ particles, but the heterogeneous oxygen diffusion track is erased after oxygen storage in the $Ce_2Zr_2O_x$ bulk. Here we show three-dimensional hard X-ray spectro-ptychography to clearly visualize the three-dimensional cerium valence map in $Ce_2Zr_2O_x$ particles, and unsupervised learning reveals the concealed oxygen-diffusion-driven three-dimensional nanoscale cerium oxidation behavior and tracking areas inside individual mixed-oxide particles during the oxygen storage process. The described approach may permit the nanoscale chemical imaging of reaction tracking areas in solid materials.

[1] Department of Engineering, Graduate School of Osaka University, Yamada-oka, Suita, Osaka 565-0871, Japan. [2] RIKEN SPring-8 Center, Kouto, Sayo-cho, Sayo, Hyogo 679-5148, Japan. [3] Japan Advanced Institute of Science and Technology, Asahidai, Nomi, Ishikawa 923-1292, Japan. [4] Department of Chemistry, Research Center for Materials Science/Graduate School of Science, Nagoya University, Furo-cho, Chikusa, Nagoya, Aichi 464-8602, Japan. [5] JST, PRESTO, 4-1-8 Honcho, Kawaguchi, Saitama 332-0012, Japan. [6] Institute of Multidisciplinary Research for Advanced Materials (IMRAM), Tohoku University, Sendai 980-8577, Japan. Correspondence and requests for materials should be addressed to H.C.D. (email: dam@jaist.ac.jp) or to M.T. (email: mtada@chem.nagoya-u.ac.jp) or to Y.T. (email: ytakahashi@tohoku.ac.jp)

Three-way exhaust catalysis is a key reaction in automobile systems[1,2], and cerium-containing mixed oxides have been widely used as support for exhaust catalysts. The oxygen storage and release capacity (OSC) of cerium-containing mixed oxides associated with the reversible oxidation and reduction of Ce^{3+} and Ce^{4+} ions enables widening of the operation window of three-way catalysts[3–5]. In particular, $Ce_2Zr_2O_x$ (denoted CZ-x, where $x = 7$–8) solid solutions with an ordered arrangement of Ce and Zr atoms exhibit remarkable OSCs[6,7]. The dynamic structural changes of CZ-x compounds with oxygen diffusion in the bulk during the redox reaction have been investigated using X-ray diffraction[8,9], neutron diffraction[10], time-resolved X-ray absorption fine structure (XAFS)[11], and theoretical calculations[12,13]. However, the reversible oxygen storage and release processes erase the oxygen diffusion track in the bulk of the CZ-x particles, and consequently the details of the oxygen storage pathways in the CZ-x particles remain unclear.

Visualization of the heterogeneity of solid catalyst particles is a state-of-the-art technology made possible by the rapid progress of X-ray imaging techniques. In particular, the combination of lens-based X-ray microscopy and XAFS spectroscopy to provide chemical state information, which makes it possible to resolve both the chemical distribution and particle structure of thick specimens with less radiation damage than that resulting from transmission electron microscopy with electron energy loss spectroscopy, is breaking new ground in materials science[14–16]. For example, scanning fluorescence/transmission X-ray microscopy has permitted two-dimensional (2D) imaging of oxygen diffusion in individual catalyst particles during oxygen storage and release[17] and captured the genesis of an active Fischer–Tropsch synthesis catalyst[18]. Full-field transmission X-ray microscopy has also revealed the three-dimensional (3D) structure and elemental distribution of an entire individual fluid catalytic cracking particle[19]. Lens-based X-ray microscopy, however, suffers from limited spatial resolution owing to the fabrication accuracy of the X-ray lens[20].

X-ray spectro-ptychography (XSP)[21], a combination of XAFS spectroscopy and X-ray ptychography[22], is a promising tool for visualizing both the structures and chemical states of bulk materials at the nanoscale beyond the limitation of the X-ray lens. In XSP, coherent X-ray diffraction patterns are collected around an absorption edge, then both the structural images and XAFS are reconstructed from the diffraction patterns via phase retrieval calculations. In this approach, the spatial resolution is determined by the maximum angular extent of the diffracted X-ray photons. 2D XSP was first demonstrated using soft X-rays[21]. The nanoscale chemical imaging of thin materials has typically been conducted in the soft X-ray realm, where the incident X-rays are mostly attenuated[23–25]. Recently, 2D XSP in the hard X-ray region has been reported, which provided 2D maps of the Ce density and valence state, suggesting the existence of several 2D domains with different oxygen storage behavior in Pt-supported CZ-x (Pt/CZ-x) catalyst particles[26]. However, significant ambiguities, especially regarding the 3D oxygen-diffusion-driven Ce oxidation tracking areas in individual CZ-x particles during the heterogeneous oxygen storage process, remain in the 2D images derived from projection of the structure and valence state along the optical axis. Recently, 3D XSP combined with computed tomography (CT) has been demonstrated in the soft X-ray region[27–29]. 3D XSP in the hard X-ray region is a promising method for visualizing the chemical states inside bulk materials such as CZ-x particles, although the huge amount of structural and chemical data in real 3D space visualized by 3D XSP necessitate the efficient extraction of key functional parameters to utilize the obtained data.

This increased volume of structural data, together with advances in machine learning and data mining techniques,

provides new opportunities for developing techniques to help researchers accelerate the discovery and comprehension of new materials and phenomena[30,31]. Supervised learning is the major machine learning method for automatically extracting the properties of materials, including their patterns and physical and chemical principles, from a database of reported information (supervisor), and this method has been utilized to construct models and previously unknown materials with optimized physical properties[30,31]. There have been numerous reports describing the application of structural imaging based on 3D tomography and supervised learning in the field of medical sciences.

The achievement of visualizing not only structures and but also chemical states of materials by spectro-imaging techniques is opening the way to extracting patterns of material properties and functions via the unsupervised learning of big imaging data[32]. Nd cluster structures in NdFeB magnets were investigated using 2D transmission X-ray microscopy coupled with XAFS and unsupervised learning[32], and different modes of crystal growths in cuprous oxide were observed upon visualization of the inhomogeneous internal electronic structures of Cu_2O particles by X-ray free-electron laser imaging with manifold learning analysis[33]. Furthermore, 3D X-ray coherent imaging of the morphology of Ti alloys was applied to predict fatigue crack growth[34]. The combination of 3D spectro-imaging techniques such as XSP, which afford not only morphological but also spatial information regarding chemical states, and unsupervised learning is a promising strategy for elucidating physical and chemical properties, which play a critical role in materials science.

Herein, we propose the approach of 3D hard X-ray spectro-ptychography (HXSP) imaging coupled with unsupervised learning to achieve the 3D nanoscale chemical imaging of heterogeneous reaction events in bulk solid materials. The 3D HXSP method allowed realization of 3D nanoscale imaging of the structure and valence state inside individual Pt/CZ-x solid solution particles during the oxygen storage process. Unsupervised data mining of the visualized 3D nanoscale chemical maps then successfully revealed the concealed heterogeneous oxygen-diffusion-driven 3D nanoscale Ce oxidation tracking areas inside the individual mixed-oxide particles during the oxygen storage process.

Results

3D HXSP nanoscale imaging of Ce valence state. Pt/CZ-x particles prepared using our previously reported method[17] were dispersed on a 200-nm-thick Si_3N_4 membrane chip. A sample reduced using H_2 at 773 K (Pt/CZ-7) was re-oxidized with O_2 at 423 K for 1 h. At this temperature, two different types of oxygen storage behavior can be observed via the metastable phase of $Ce_2Zr_2O_{7.5}$ (CZ-7.5)[17], and 3D HXSP imaging is regarded to reflect the 3D oxidation reaction tracking of the oxidation (oxygen storage) process.

3D HXSP (5.708–5.770 keV, which includes the Ce L_{III}-edge) was conducted at the SPring-8 BL29XUL beamline, and a schematic representation of the 3D HXSP measurement is presented in Fig. 1. For the CT measurement, the sample was rotated from −75 to 75° via 61 evenly spaced angles at each X-ray energy. The projected amplitude and phase images at each angle were reconstructed using the ePIE algorithm[35] with the Kramers–Kronig relation (KKR) constraint[36]. Then, 3D image reconstruction was accomplished using the filtered back projection (FBP) algorithm at each X-ray energy. The voxel size of the reconstructed 3D HXSP images in real space was as low as 14 nm, in contrast to the size of single CZ-x particles of ~500 nm to 1 µm, enabling the determination of the 3D oxidation reaction tracking
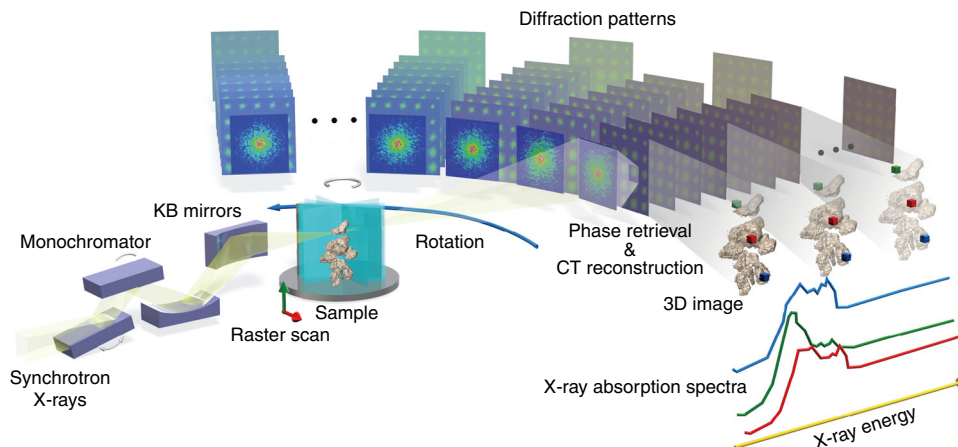
Fig. 1 Schematic representation of 3D HXSP. Synchrotron X-rays are monochromatized using a Si(111) double-crystal monochromator. The monochromatic X-rays are two-dimensionally focused using a pair of KB mirrors. A sample placed at the focal plane is laterally scanned across the illumination field. Coherent X-ray diffraction patterns are collected as a function of both the incident X-ray energy and angle. The projected amplitude and phase images at each angle and each energy are reconstructed, followed by 3D image reconstruction

areas in individual catalyst particles during the oxygen storage process.

Figure 2a shows the isosurface rendering of the reconstructed 3D HXSP phase images of six CZ-x particles in the field of view. The facet structures on the surfaces of the CZ-x particles can be clearly visualized in the 3D HXSP image. The Ce L_{III}-edge ptychographic-XAFS spectra (Fig. 2b) allowed discrimination of Ce^{3+} and Ce^{4+}, whose linear combination fitting at each voxel afforded a 3D map of the Ce oxidation state in (x,y,z) real space (Supplementary Movie 1). The resulting 3D cross-sectional images of the Ce valence are presented in Fig. 2c, showing the heterogeneous variation of the Ce oxidation state inside individual CZ-x particles where oxygen storage partially proceeded via the oxidation of CZ-7 with O_2 at 423 K for 1 h. The surfaces of the solid particles appeared blue (Ce^{4+}) and wide color variation inside the solid particles was observed in a heterogeneous manner.

Histograms of the Ce valence for each of the six CZ-x particles are presented in Fig. 2d. Particles 5 and 6 exhibited a histogram peak around the Ce valence state of $+3.5$. Particles 1, 2, and 4 displayed similar histograms with a peak around $+3.6$ in addition to a peak around $+4.0$. Particle 3 exhibited a continuous broad histogram with a vague peak around $+3.6$. Most of the particles shown in Fig. 2d afforded histograms with a plateau around $+3.85$. There were no voxel domains of Ce valence states lower than ~$+3.5$ for any of the CZ-x particles 1–6. The results for the 3D mapping analysis of the 14 nm voxel domains in Fig. 2c and d reveal the 3D tracking areas of the metastable phase of CZ-7.5 ($Ce_2Zr_2O_{7.5}$) with the unique $Ce^{3.5+}$ mixed valence[8,9] and demonstrate the kinetically faster oxidation of the CZ-7 phase (Ce^{3+}) with oxygen vacancies to the CZ-7.5 phase ($Ce^{3.5+}$), compared with the subsequent oxidation of the CZ-7.5 phase, during the partial oxygen storage process at 423 K for 1 h. This first report of 3D nanoscale HXSP imaging provides a deeper understanding than the previous micrometer-scale (optical depth) averaged analysis of the Ce density–valence relationship by 2D HXSP[26].

Unsupervised learning of the 3D nanoscale valence map. The 3D HXSP imaging results provided a 3D nanoscale Ce valence map of the solid particles with $452 \times 450 \times 136$ voxels. We considered each voxel as a data instance, giving a dataset of 27,662,400 Ce valence data instances for the six CZ-x particles for

data mining of the patterns of Ce valence in the particles during the oxygen storage process. The process used to find correlations between parameters in the visualized 3D maps was unsupervised learning.

To characterize each voxel, we considered the surrounding binning of $3 \times 3 \times 3$ voxels ($42 \times 42 \times 42$ nm^3) in the 3D map and used the local mean ($m(x,y,z)$) and local standard deviation ($sd(x,y,z)$) of the Ce valence state in each binning domain as descriptors. Note that $m(x,y,z)$ corresponds to the degree of oxygen storage ($Ce^{3+} \rightarrow Ce^{4+}$) and $sd(x,y,z)$ corresponds to the variation of oxygen storage in the local domains. Using these descriptors, we observed a volcano-type correlation between $m(x,y,z)$ and $sd(x,y,z)$, as shown in Fig. 3a. The distribution in the 2D $m(x,y,z)$-$sd(x,y,z)$ plot was approximated by a mixture model of K Gaussian distributions, and an expectation–maximization algorithm[37] was adopted for parameter estimation. By minimizing the Bayesian information criterion[38], the number of components in the 2D $m(x,y,z)$-$sd(x,y,z)$ plot was determined.

Note that the Gaussian mixture model approximating the 2D plot of (m, sd) revealed that the actual distribution of the entire dataset $\mathcal{D}$ was a mixture of four Gaussian components denoted G_1, G_2, G_3, and G_4 with respect to the set of the following centers $\boldsymbol{\mu} = \{(3.43, 0.143), (3.61, 0.265), (3.85, 0.224), \text{ and } (3.97, 0.063)\}$ and covariance matrices $\boldsymbol{\Sigma} = \{[(0.02766, -0.00078), (-0.00078, 0.00221)], [(-0.02076, -0.00351), (-0.00351, 0.00837)], [(0.00478, -0.00441), (-0.00441, 0.00729)], \text{ and } [(0.00057, -0.00114), (-0.00114, 0.00252)]\}$, respectively (Fig. 3a). The main significance of the unsupervised data mining procedure was to determine the most likely number of reaction stages during the oxygen storage process from the visualized 3D map. Taking into account that the horizontal axis $m(x,y,z)$ denotes the degree of oxygen storage, the red component G_1 corresponds to the domains where oxygen storage did not proceed for the most part but brought about a distribution of Ce valence states with a maximum probability around the CZ-7.5 phase during the oxygen storage process at 423 K for 1 h. The orange component G_2 corresponds to the domains where oxygen storage proceeded beyond the CZ-7.5 phase but displayed a large data variation. The green component G_3 corresponds to the domains where oxygen storage converged to the final state of CZ-8 containing Ce^{4+}. The blue component G_4 corresponds to the domains where oxygen storage was almost complete and displayed the smallest standard deviation. Thus, the 2D scattering plot of the mean Ce valence (m) and its standard deviation (sd) in the
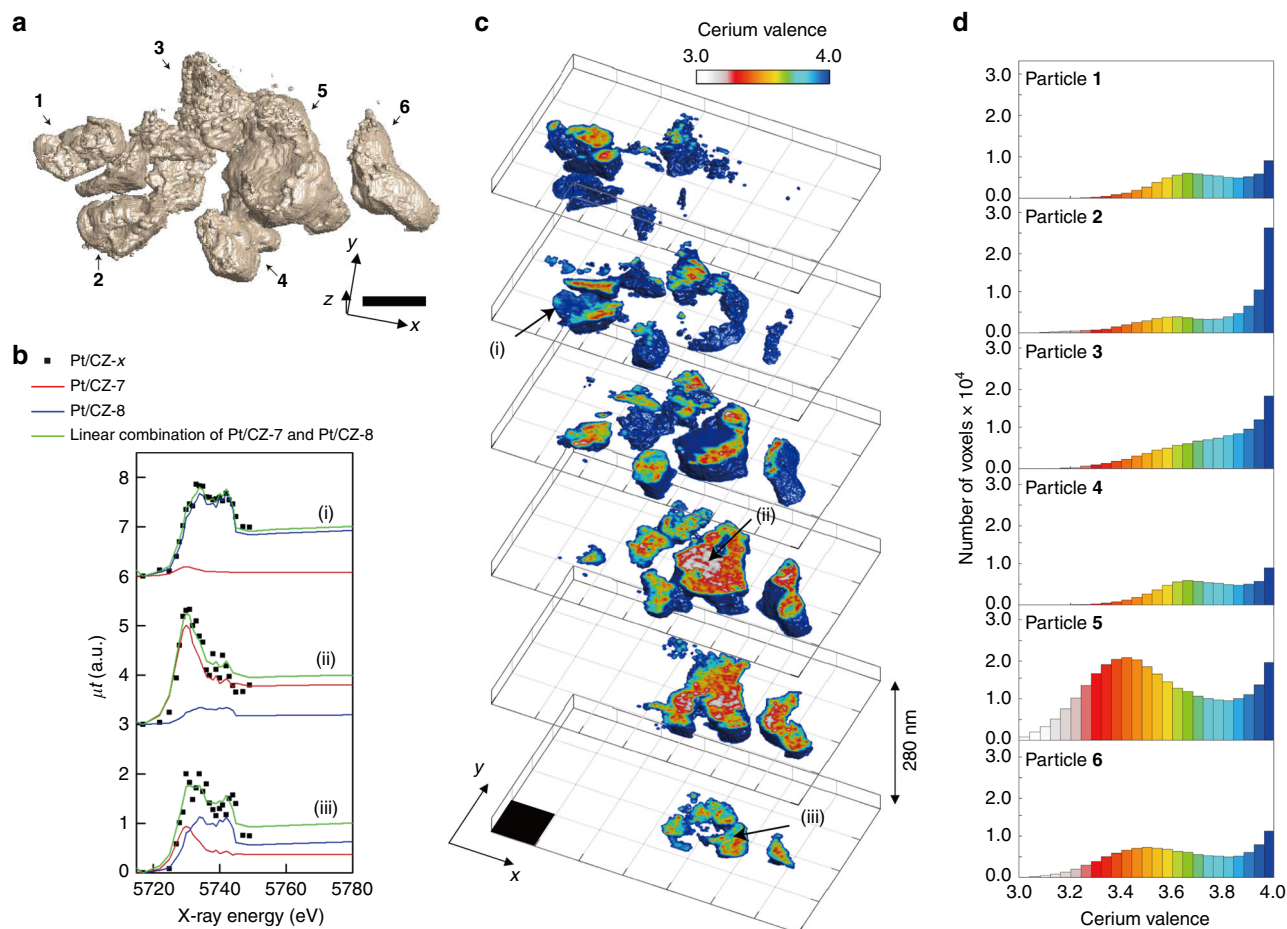
Fig. 2 3D mapping and XAFS analysis. **a** Isosurface rendering of the reconstructed 3D phase map of partially oxidized Pt/CZ particles. The scale bar is 700 nm. **b** Three-dimensionally resolved XAFS spectra and their fitted spectra. The green spectra are the results of the linear combination of the XAFS spectra of Pt/CZ-7 (red) and Pt/CZ-8 (blue) normalized at the isosbestic point of 5.7697 keV. The black dots (i), (ii), and (iii) are the XAFS signals extracted from the $56 \times 56 \times 56\ nm^3$ volumes indicated at (i), (ii), and (iii) in **c**. **c** Series of slices of the 3D Ce valence image along the z direction. The black square represents $700 \times 700\ nm^2$. **d** Ce valence distributions for the number of voxels of the particles labeled in **a**

$42 \times 42 \times 42\ nm^3$ ($3 \times 3 \times 3$ voxels) domains of partially oxidized Pt/CZ-x particles exhibited a volcano-type pattern as shown in Fig. 3a, which was related to the course of the oxygen storage process during Ce oxidation from Ce^{3+} to Ce^{4+} via the G_1, G_2, and G_3 domains in the CZ-x particles concealed in the bulk. The Ce oxidation in the G_1 domains proceeds in the CZ-7 phase with a pyrochlore structure, whereas the Ce oxidation in the G_2 domains around $+3.61$ is regarded to occur in the disordered (mixed) phases accompanied by the transformation of the pyrochlore phase to the CZ-8 κ-phase with a fluorite structure and showing a larger sd. Further oxygen storage proceeds in the Ce oxidation states above $+3.7$ and forms the G_3 domains with a maximum Ce valence population around $+3.85$. The G_3 domains, considered nearly a fluorite phase, readily converge to the Ce^{4+} valence state in the G_4 domains and the final CZ-8 phase.

We classified the locations of the four groups (G_1, G_2, G_3, and G_4) in (x,y,z) real space and present a 3D map and cross-sectional images in Fig. 3b, c, respectively. These figures clearly demonstrate that the locations of the four groups were dependent on the morphological characteristics of the particles: the domains belonging to G_4 (blue) were observed at the outermost surfaces of the particles, whereas those belonging to G_1 (red) were predominantly located in the cores of the particles. Similar differences in the 3D Ce valence images of the particles were observed in Fig. 2c. Recently, we reported five different types of

correlations between the Ce density and Ce valence (positive, negative, quasi-constant to Ce density, quasi-constant to Ce valence, and no correlation) in 2D HXSP images[26]; the G_1 group can be related to the positive correlation between Ce density and Ce valence that was observed for Ce valences lower than $+3.5$ and near the centers of the particles, whereas the G_3 and G_4 groups can be related to the negative correlation that was observed for Ce valences of $+3.5$ to $+4.0$ and around the surfaces of the particles in the 2D images. However, the five different types of oxidation behavior in the local domains of the CZ-x particles described in the previous report[26] were determined from the correlations in 2D images averaged over the entire depth direction of the local domains (along the optical axis), where the 2D data for the local domains may be merged with and obfuscated by the data at minor heterogeneous sites of the particles, such as boundaries, defects, and interfaces, although the 2D HXSP image analysis successfully revealed the 2D distribution of Ce oxidation states inside the catalyst particles[26]. The current 3D HXSP image rendering is the first report of the 3D visualization of the nanoscale oxidation tracking areas in CZ-x catalyst particles during the oxygen storage process.

The geometric distance between each domain and the outermost surface of a particle was calculated from the 3D HXSP image and the fractions for the four groups were plotted against the distance from the surface (Fig. 3d). The G_1 domains with
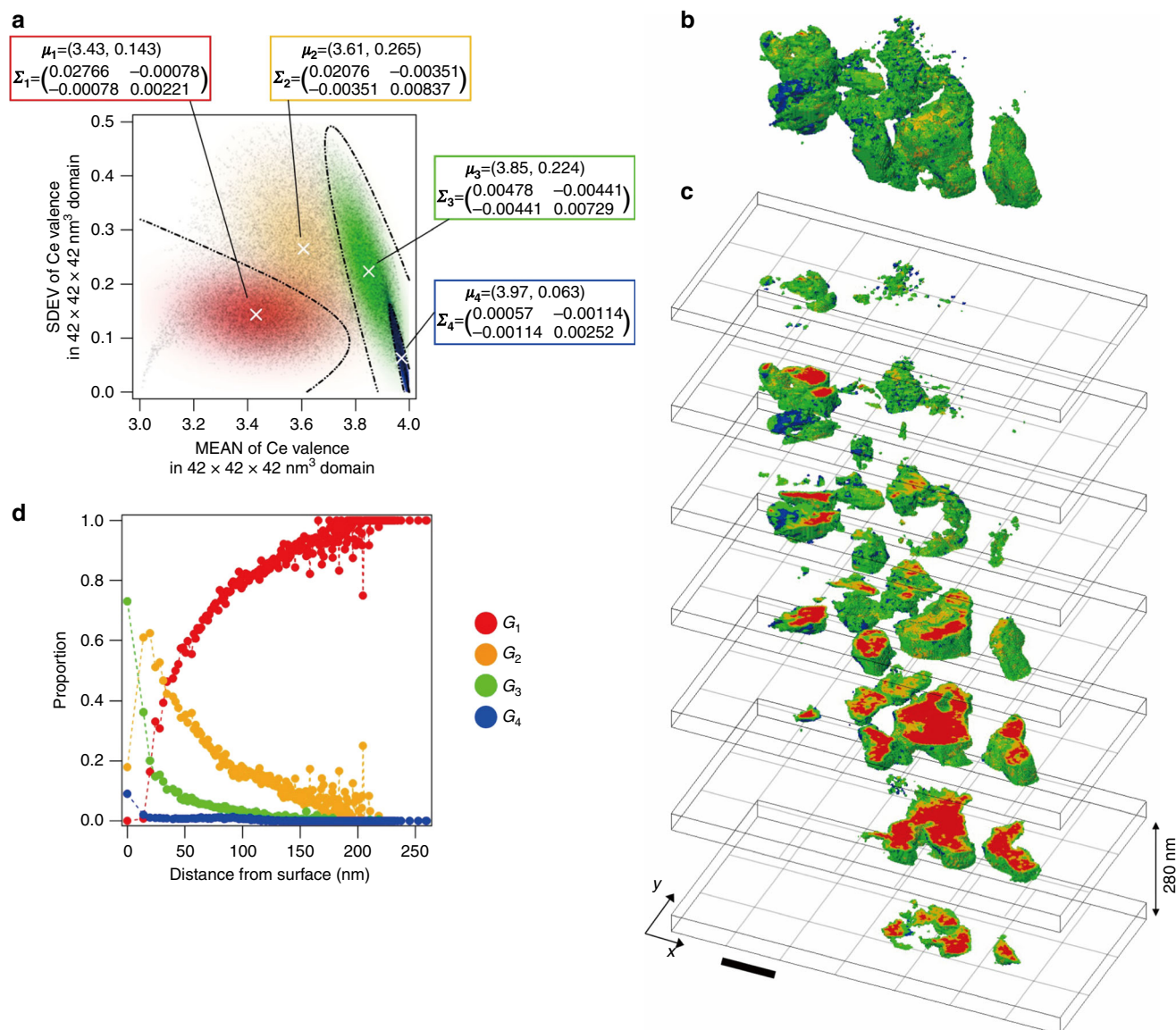
Fig. 3 Unsupervised learning analysis of the 3D Ce valence map. **a** Scatter plot of mean Ce valence (m) and its standard deviation (sd) for $42 \times 42 \times 42$ nm^3 ($3 \times 3 \times 3$ voxels) domains of partially oxidized Pt/CZ-x particles, and classification of correlation trends using a Gaussian mixture model. Red: G_1; orange: G_2; green: G_3; blue: G_4. The white crosses indicate the Gaussian centers for G_1–G_4; μ_k ($k = 1$–4): Gaussian center; Σ_k: covariance matrix. **b** 3D rendering of the distribution of the four correlation groups between m and sd for $42 \times 42 \times 42$ nm^3 ($3 \times 3 \times 3$ voxels) domains of partially oxidized Pt/CZ-x particles, and **c** series of slices showing the 3D distributions of the four correlation groups along the z direction. The scale bar for **b** and **c** is 700 nm. **d** Plot of the proportion of each correlation group in **c** with respect to distance from the particle surface

limited oxidation did not appear within 20 nm of the outer surfaces of the particles and their fraction greatly increased toward the bulk of the particles. The G_2 domains exhibited a maximum proportion at 20 ± 17 nm, which gradually decreased over 200 nm toward the bulk. Considering the stable surfaces of the fluorite/pyrochlore structures (e.g., (111) or (110))[39,40], the maximum proportion (20 nm) of G_2 corresponded to a depth of ~40–50 oxygen vacancy sites from the surface of the particles. The G_3 domains with considerable oxidation were located at the surface regions of the particles and their fraction showed a rapid exponential decrease up to 25 nm followed by a gentle decrease over 100 nm toward the core. The G_4 domains with a valence of ~+4.0 were located at the surface layer (<20 nm), although it should be noted that these were a minor component and the surface region was composed of greater fractions of the G_3 and G_2 domains. These results demonstrate that achieving the complete oxidation of Ce^{3+} to Ce^{4+} throughout the entire surface

region is difficult during the oxygen storage process at 423 K for 1 h.

The parameter $sd(x,y,z)$ corresponds to the spatial gradient of the Ce valence distribution, which is related to oxygen diffusion in the CZ-x particles. As the oxygen is supplied from the surfaces of the particles, the four groups plotted in Fig. 3a reveal the nature of the oxygen diffusion in the CZ-x particles from the surface to the bulk during the oxygen storage process. During the first stage (G_1), there are many vacant sites in the CZ-7 particles with the pyrochlore structure and oxygen can diffuse smoothly through the vacant oxygen sites. Following the formation of a heterogeneous distribution of vacant oxygen sites in the intermediate phase of CZ-7.5 (the second stage, G_2), further oxygen storage occurs and is completed through the third stage (G_3) to the final stage (G_4). Although macroscopic analysis of CZ particles during oxygen storage via temperature-programmed oxidation and thermogravimetry previously suggested a two-step

oxidation mechanism for the oxygen storage process via CZ-7.5[8,9], it is noteworthy that the present static 3D imaging and unsupervised data mining have opened up the possibility of visualizing the nanoscale tracking areas of the reaction course with local heterogeneity in the reactivity inside solid catalyst particles.

Discussion

3D XSP in the hard X-ray region permitted successful visualization of the 3D distribution of the Ce oxidation states in Pt/CZ-x exhaust catalyst particles with a 3D sampling pitch of 14 nm. Data mining of the 3D HXSP images of the Ce valence revealed four groups related to the morphological characteristics and local reactivity for oxygen storage, elucidating the oxidation pathways occurring in the solid catalyst. 3D HXSP is expected to be an indispensable tool for determining reaction tracking areas and the relationships between the structure and function of heterogeneous functional materials. In particular, in next-generation synchrotron facilities where fluxes with much higher coherence will be achieved, the present approach will be applied to in situ 3D measurements, which can be expected to significantly accelerate progress in chemistry and materials science.

Methods

Sample preparation. The sample of Pt/CZ-x particles was prepared by the reported method[6,17,41,42]. $Ce_2Zr_2O_8$ particles were obtained by a method reported by Toyota Central R&D Labs. Inc., from aqueous solutions of $Ce(NO_3)_3 \cdot 6H_2O$ and $ZrO(NO_3)_2 \cdot 2H_2O$. 1% of Pt ($Pt(NH_3)_4(NO_3)_2$) was impregnated on $Ce_2Zr_2O_8$ and calcined at 773 K for 1 h to obtain Pt/CZ-8.

About 3 mg of the prepared Pt/CZ-8 was suspended in 10 mL of absolute ethanol by ultrasonic treatment, then 1 μL of the suspension was dispersed on a 200-nm-thick Si_3N_4 membrane chip (NORCADA Inc.). The Si_3N_4 membrane with the Pt/CZ-x particles was treated in a H_2 flow (99.99999%, 1 bar, 60 mL min^{-1}) at 773 K for 2 h and Pt/CZ-7/Si_3N_4 was obtained. Then, the obtained Pt/CZ-7/Si_3N_4 was treated in an O_2 flow (99.99999%, 1 bar, 60 mL min^{-1}) at 423 K for 1 h to obtain the partially oxidized Pt/CZ-x sample[17]. The dispersion of the particles on the membrane was evaluated by SEM (HITACHI, S-4800) (Supplementary Fig. 1a).

3D HXSP measurements. 3D HXSP measurements were performed at the BL29XUL undulator beamline at SPring-8, Japan. Twenty-eight X-ray energies between 5.708 and 5.770 keV were used at the Ce-L_{III} edge with a Si(111) double-crystal monochromator. The finest energy gap was 1 eV (between 5.727 and 5.744 keV). The monochromatized X-rays were two-dimensionally focused to a spot size of 500 nm full-width at half-maximum using a pair of Kirkpatrick–Baez (KB) mirrors. Owing to the achromatic property of the KB mirrors, the focusing position was invariant with respect to the X-ray energy. The sample was mounted on the piezoelectric stages in a vacuum chamber and scanned in an 8 × 8 grid with a 400 nm step size. The diffraction patterns were measured with exposure times ranging from 0.5 to 4.0 s using a pixel array detector (EIGER 1M, Dectris) with a pixel size of 75 μm positioned 2.219 m downstream of the sample. To increase the effective dynamic range of the diffraction intensity, an 800 × 800 × 88 μm^3 Si attenuator was placed in front of the central region of the detector. For the CT measurements, the sample was rotated from −75 to 75° via 61 evenly spaced angles for each X-ray energy. The total data acquisition required 5 days, including the energy scan, sample rotation, and experimental interruptions.

3D image reconstruction. The 2D image reconstructions were accomplished using the ePIE algorithm[35] with the KKR constraint[36] at each orientation (Supplementary Fig. 1b–e). The full-period spatial resolution of the projected images was estimated to be superior to 30 nm at the longest exposure and 50 nm at the shortest exposure on the basis of phase retrieval transfer function (PRTF) analysis (Supplementary Fig. 2a, b). Next, 3D image reconstruction was performed using the FBP algorithm at each X-ray energy. The 3D spatial resolution was better than 60 nm, which was ascertained on the basis of the edge structures (Supplementary Fig. 3). The 3D Ce valence maps of the particles were determined by analyzing the HXSP images. The XAFS spectra of Pt/CZ-x (μt)$_{CZ-x}$ can be approximately expressed by a linear combination of the normalized XAFS spectra of Pt/CZ-7 (μt)$_{CZ-7}$ and Pt/CZ-8 (μt)$_{CZ-8}$ as follows:

$$(\mu t)_{CZ-x} = a(\mu t)_{CZ-7} + b(\mu t)_{CZ-8}, \qquad (1)$$

where a and b are coefficients. The parameters a and b at each voxel were determined using a least-squares fit in the energy range between 5.718 and 5.749 keV. $(3a+4b)/(a+b)$ corresponds to the Ce valence. The average R factor over all of the voxels in particle 5 was calculated to be 0.0823.

Unsupervised learning. We considered the surrounding binning of 3 × 3 × 3 voxels (42 × 42 × 42 nm^3) in the 3D Ce valence map and used the local mean ($m(x, y,z)$) and local standard deviation ($sd(x,y,z)$) of the Ce valence state in each binning domain as descriptors. We then obtain a dataset $\mathcal{D}$ that contains the information of all the observed voxels. A voxel with index i in $\mathcal{D}$ is described by the 2D vector $\mathbf{x}_i = (m_i, sd_i)$; therefore, the dataset $\mathcal{D}$ is represented using an ($n \times 2$) matrix. The distribution was approximated by a mixture models of K Gaussian distributions[37] (Supplementary Fig. 4) as follows:

$$p(\mathbf{x}_i | \boldsymbol{\theta}) = \sum_{k=1}^{K} \pi_k \mathcal{N}(\boldsymbol{\mu}_k, \boldsymbol{\Sigma}_k) \qquad (2)$$

where $\boldsymbol{\pi}$, $\boldsymbol{\mu}$, and $\boldsymbol{\Sigma}$ are the weights, centers, and coefficient matrices for the 2D Gaussians, respectively. For a given number of mixture component K, the estimation of the parameter is conducted through an expectation-maximization algorithm[37]. To determine the number of mixture components, a minimizing Bayesian information criterion[38] process is utilized that involves applying several different trials to randomize the initial states. We have tried to approximate the distribution of dataset $\mathcal{D}$ by mixture models of K (= 1, 2, 3, 4, 5, 6) Gaussian distributions. For K (= 1, 2, 3, 4), we can obtain significant improvement in the Bayesian information criterion of the approximation. However, for K (= 4, 5, 6), the Bayesian information criterion of the approximation does not improve significantly. We therefore determine the number of mixture components at four components. As a result, the whole dataset $\mathcal{D}$ on the representation space (m, sd) is divided into four Gaussian components G_1, G_2, G_3, G_4 with respect to the set of the following parameters: $\boldsymbol{\pi}$ = {0.329, 0.319, 0.262, 0.091}, $\boldsymbol{\mu}$ = {(3.43, 0.143), (3.61, 0.265), (3.85, 0.224), (3.97, 0.063)}, $\boldsymbol{\Sigma}$ = {[(0.02766, −0.00078), (−0.00078, 0.00221)], [(0.02076, −0.00351), (−0.00351, 0.00837)], [(0.00478, −0.00441), (−0.00441, 0.00729)], [(0.00057, −0.00114), (−0.00114, 0.00252)]}.

Data availability

The authors declare that all data supporting the findings of this study are available within the paper or are available from the authors upon request.

References

1. Ertl, G., Knözinger, H., Schüth, F. & Weitkamp, J. *Handbook of Heterogeneous Catalysis*, 2nd edn (Wiley-VCH, Weinheim, 2008).
2. Mitchell, S., Michels, N. L. & Pérez-Ramírez, J. From powder to technical body: the undervalued science of catalyst scale up. *Chem. Soc. Rev.* **42**, 6094–6112 (2013).
3. Yao, H. C. & Yao, Y. F. Y. Ceria in automotive exhaust catalysts. *J. Catal.* **86**, 254–265 (1984).
4. Kašper, J., Fornasiero, P. & Graziani, M. Use of CeO$_2$-based oxides in the three-way catalysis. *Catal. Today* **50**, 285–298 (1999).
5. Matsumoto, S. Recent advances in automobile exhaust catalysts. *Catal. Today* **90**, 183–190 (2004).
6. Suda, A., Ukyo, Y., Sobukawa, H. & Sugiura, M. Improvement of oxygen storage capacity of CeO$_2$-ZrO$_2$ solid solution by heat treatment in reducing atmosphere. *J. Ceram. Soc. Jpn* **110**, 126–130 (2002).
7. Urban, S. et al. In situ study of the oxygen-induced transformation of pyrochlore Ce$_2$Zr$_2$O$_{7+x}$ to the κ-Ce$_2$Zr$_2$O$_8$ phase. *Chem. Mater.* **29**, 9218–9226 (2017).
8. Sasaki, T. et al. Crystal structure of Ce$_2$Zr$_2$O$_7$ and β-Ce$_2$Zr$_2$O$_{7.5}$. *J. Ceram. Soc. Jpn.* **112**, 440–444 (2004).
9. Sasaki, T. et al. Oxygen absorption behavior of Ce$_2$Zr$_2$O$_{7+x}$ and formation of Ce$_2$Zr$_2$O$_{7.5}$. *J. Ceram. Soc. Jpn* **111**, 382–385 (2003).
10. Achary, S. N. et al. Intercalation/deintercalation of oxygen: a sequential evolution of phases in Ce$_2$O$_3$/CeO$_2$−ZrO$_2$ pyrochlores. *Chem. Mater.* **21**, 5848–5859 (2009).
11. Yamamoto, T. et al. Origin and dynamics of oxygen storage/release in a Pt/ordered CeO$_2$−ZrO$_2$ catalyst studied by time-resolved XAFS analysis. *Angew. Chem. Int. Ed.* **46**, 9253–9256 (2007).
12. Wang, H. F., Guo, Y. L., Lu, G. Z. & Hu, P. Maximizing the localized relaxation: the origin of the outstanding oxygen storage capacity of κ-Ce$_2$Zr$_2$O$_8$. *Angew. Chem. Int. Ed.* **48**, 8289–8292 (2009).
13. Gupta, A., Kumar, A., Waghmare, U. V. & Hedge, M. S. Activation of oxygen in Ce$_2$Zr$_2$O$_{7+x}$ across pyrochlore to fluorite structural transformation: first-principles analysis. *J. Phys. Chem. C* **121**, 1803–1808 (2017).
14. Smit, E. et al. Nanoscale chemical imaging of a working catalyst by scanning transmission X-ray microscopy. *Nature* **456**, 222–225 (2008).
15. Buurmans, I. L. C. & Weckhuysen, B. M. Heterogeneities of individual catalyst particles in space and time as monitored by spectroscopy. *Nat. Chem.* **4**, 873–886 (2012).

16. Meirer, F. & Weckhuysen, B. M. Spatial and temporal exploration of heterogeneous catalysts with synchrotron radiation. *Nat. Rev. Mater.* **3**, 324–340 (2018).

17. Matsui, H. et al. Imaging of oxygen diffusion in individual platinum/Ce$_2$Zr$_2$O$_x$ catalyst particles during oxygen storage and release. *Angew. Chem. Int. Ed.* **55**, 12022–12025 (2016).

18. van Ravenhorst, I. K. et al. Capturing the genesis of an active Fischer-Tropsch synthesis catalyst with operando X-ray nanospectroscopy. *Angew. Chem. Int. Ed.* **57**, 11957–11962 (2018).

19. Meirer, F. et al. Mapping metals incorporation of a whole single catalyst particle using element specific X-ray nanotomography. *J. Am. Chem. Soc.* **137**, 102–105 (2015).

20. Miao, J., Ishikawa, T., Robinson, I. K. & Murnane, M. M. Beyond crystallography: diffractive imaging using coherent x-ray light sources. *Science* **348**, 530–535 (2015).

21. Shapiro, D. A. et al. Chemical composition mapping with nanometre resolution by soft X-ray microscopy. *Nat. Photonics* **8**, 765–769 (2014).

22. Rodenburg, J. M. et al. Hard-X-ray lensless imaging of extended objects. *Phys. Rev. Lett.* **98**, 034801 (2007).

23. Yu, Y. S. et al. Dependence on crystal size of the nanoscale chemical phase distribution and fracture in Li$_x$FePO$_4$. *Nano Lett.* **15**, 4282–4288 (2015).

24. Wise, A. M. et al. Nanoscale chemical imaging of an individual catalyst particle with soft X-ray ptychography. *ACS Catal.* **6**, 2178–2181 (2016).

25. Zhu, X. et al. Measuring spectroscopy and magnetism of extracted and intracellular magnetosomes using soft X-ray ptychography. *Proc. Natl Acad. Sci. USA* **113**, E8219–E8227 (2016).

26. Hirose, M. et al. Visualization of heterogeneous oxygen storage behavior in platinum-supported cerium-zirconium oxide three-way catalyst particles by hard X-ray spectro-ptychography. *Angew. Chem. Int. Ed.* **130**, 1490–1495 (2018).

27. Yu, Y. S. et al. Three-dimensional localization of nanoscale battery reactions using soft X-ray tomography. *Nat. Commun.* **9**, 921 (2018).

28. Wu, J. et al. High-resolution imaging of polymer electrolyte membrane fuel cell cathode layers by soft X-ray spectro-ptychography. *J. Phys. Chem. C* **122**, 11709–11719 (2018).

29. Wu, J. et al. Four-dimensional imaging of ZnO-coated alumina aerogels by scanning transmission X-ray microscopy and ptychographic tomography. *J. Phys. Chem. C* **122**, 25374–25385 (2018).

30. Isayev, O. et al. Materials cartography: representing and mining materials space using structural and electronic fingerprints. *Chem. Mater.* **27**, 735–743 (2015).

31. Ghiringhelli, L. M., Vybiral, J., Levchenko, S. V., Draxl, C. & Scheffler, M. Big data of materials science: critical role of the descriptor. *Phys. Rev. Lett.* **114**, 105503 (2015).

32. Duan, X. et al. Unsupervised data mining in nanoscale X-ray spectro-microscopic study of NdFeB magnet. *Sci. Rep.* **6**, 34406 (2016).

33. Oroguchi, T., Yoshidome, T., Yamamoto, T. & Nakasako, M. Growth of cuprous oxide particles in liquid-phase synthesis investigated by X-ray laser diffraction. *Nano Lett.* **18**, 5192–5197 (2018).

34. A. Rovinelli, M. et al. Predicting the 3D fatigue crack growth rate of small cracks using multimodal data via Bayesian networks: in-situ experiments and crystal plasticity simulations. *J. Mech. Phys. Solids* **115**, 208–229 (2018).

35. Maiden, A. M. & Rodenburg, J. M. An improved ptychographical phase retrieval algorithm for diffractive imaging. *Ultramicroscopy* **109**, 1256–1262 (2009).

36. Hirose, M., Shimomura, K., Burdet, N. & Takahashi, Y. Use of Kramers–Kronig relation in phase retrieval calculation in X-ray spectro-ptychography. *Opt. Express* **25**, 8593–8603 (2017).

37. Murphy, K. P. *Machine Learning: A Probabilistic Perspective* (MIT Press, Cambridge, 2012).

38. Schwarz, G. Estimating the dimension of a model. *Ann. Stat.* **6**, 461–464 (1978).

39. Dholabhai, P. P., Perriot, R. & Uberuaga, B. P. Atomic-scale structure and stability of the low-index surfaces of pyrochlore oxides. *J. Phys. Chem. C* **120**, 10485–10499 (2016).

40. López-Haro, M. et al. Advanced electron microscopy investigation of ceria–zirconia–based catalysts. *ChemCatChem* **3**, 1015–1027 (2011).

41. Tada, M. et al. The active phase of nickel/ordered Ce$_2$Zr$_2$O$_x$ catalysts with a discontinuity ($x = 7$-8) in methane steam reforming. *Angew. Chem. Int. Ed.* **51**, 9361–9365 (2012).

42. Tada, M. et al. µ-XAFS of a single particle of a practical NiO$_x$/Ce$_2$Zr$_2$O$_y$ catalyst. *Phys. Chem. Chem. Phys.* **13**, 14910–14913 (2011).

Acknowledgements

Author contributions

M.H., K.S., and Y.T. performed the synchrotron experiments. M.H. performed the image reconstructions. M.H. and H.M. prepared the samples. M.H. performed the SEM observations of the samples. D.N.N. and H.C.D. performed the data mining analysis. M. T. and N.I. interpreted the results. M.H., N.I., H.C.D., H.M., M.T., and Y.T. wrote the manuscript. All authors read and approved the manuscript.

Additional information

Supplementary information accompanies this paper at https://doi.org/10.1038/s42004-019-0147-y.

Competing interests: The authors declare no competing interests.

Reprints and permission information is available online at http://npg.nature.com/reprintsandpermissions/

Publisher's note: Springer Nature remains neutral with regard to jurisdictional claims in published maps and institutional affiliations.